Investigation of Physical Mechanisms for Jet Noise Reduction by Plug Nozzle Porosity

John Henry Korth[1], Jonathan M. Burt[2], Khairul B. M. Q. Zaman[3] and Amy Fagan[4],
NASA Glenn Research Center, Cleveland, OH, 44135

This paper presents the results of a computational and experimental study on porous plug nozzles and the fluid mechanisms surrounding their observed noise reduction. The study explores a wide range of porous plug geometries, encompassing variations in hole size, plug length and porosity. Computational fluid dynamics (CFD) analyses are employed in concert with an advanced automated mesh refinement (AMR) scheme to investigate porous plug nozzle design strategies that may diminish shock strength, flow separation, and other undesirable characteristics associated with high noise levels. A selected subset of the porous plug nozzles that were analyzed computationally were fabricated at subscale and tested experimentally, obtaining far-field noise spectral data and schlieren flow visualizations. Detailed comparisons between CFD predictions and experimental results were focused on gaining an improved understanding of underlying physical mechanisms responsible for noise reduction associated with the porous plugs.

I. Introduction

Excessive airport noise remains a major barrier to regulatory approval and public acceptance of supersonic commercial aircraft [1]. Takeoff noise, primarily driven by jet exhaust [2], is exacerbated by high thrust requirements and low bypass ratios of turbofan engines optimized for supersonic cruise. Operational strategies including engine derating and variable noise reduction systems [3] offer partial mitigation, while hardware-based solutions such as chevrons [4], mechanical shielding [3], multi-stream nozzles [4], mixer-ejectors [5], and plug nozzles [6, 7] have been explored. However, none of these achieve sufficient noise reduction for regulatory compliance without excessive complexity or substantial efficiency losses [1]. The lack of adequate noise reduction via current strategies motivates current research into alternate approaches for jet noise reduction.

One promising but underexplored approach for jet noise reduction on supersonic aircraft is the porous external plug nozzle. In this approach, which is based on the altitude-compensating plug nozzle configuration that is commonly used in conceptual supersonic vehicle designs, a series of small holes are positioned along the plug surface downstream of the throat, allowing flow exchange between an internal cavity and the exhaust. This passive circulation mechanism can weaken shock interactions between the plug and the nearfield mixing layer, reducing various aberrant noise components, e.g., broadband shock-associated noise (BBSN). Conventional nonporous plug nozzles generate conical shocks (in overexpanded flow) or expansion fans (in underexpanded flow) from the cowl lip, which reflect between the outer shear layer and the plug surface, forming a shock train. In recent experiments, Zaman et al. [6] demonstrated significant BBSN reduction with a conical porous plug nozzle at jet Mach number (MJ) = 1.38, showing weaker shock reflections in schlieren images. However, the effectiveness of plug porosity varies with

---

[1] Research Aerospace Engineer, Inlets and Nozzles Branch.
[2] Research Aerospace Engineer, Propulsion Systems Analysis Branch; AIAA Associate Fellow.
[3] Research Aerospace Engineer, Inlets and Nozzles Branch; AIAA Associate Fellow.
[4] Research Aerospace Engineer, Optics & Photonics Branch; AIAA Associate Fellow.

nozzle geometry, jet Mach number, and nozzle pressure ratio (NPR). Further studies [7] reveal additional sensitivity to cowl shape and other geometric parameters.

This study uses computational fluid dynamics (CFD) and subscale experiments to evaluate the geometric dependencies of porous plug nozzles on shock reduction. Building on prior experiments [6, 9], Reynolds-averaged Navier-Stokes (RANS) simulations with the FUN3D solver [10] are employed to systematically assess design sensitivities of the flowfield. The work extends an earlier study [8] on optimized nonporous plug design for takeoff and cruise efficiency, with ultimate objectives to identify the physical mechanisms governing shock and shock-associated noise reduction, and to inform future noise-mitigating nozzle designs for supersonic aircraft.

II. Geometry

For the CFD-based assessment performed as part of this work, porosity pattern and hole geometry modifications were applied to a fixed nozzle configuration with an internal cowl radius (r_c) of 1 in., focusing on the porous plug section from crown to tip while keeping the upstream and cowl geometry unchanged. Plugs were generated at three values of the length factor (*LF*), defined as the axial crown-to-tip plug length normalized by a baseline length of 2.421 in. Cases included a nominal case *LF=1* based on previous 2D CFD-informed design optimization [8], as well as shorter *LF=0.7* and longer *LF=1.3* profiles obtained by linearly scaling the nominal profile in the axial (*x*) direction. Plug porosity (φ) is defined as the open area fraction of the plug surface. Each porosity pattern was defined by the target porosity (φ_{target}) and hole radius (r_{hole}) with φ_{target} values of 0%, 5%, 10% and 15%. Hole spacing (s_{target}) was iteratively adjusted to match φ_{target} constrained by quarter-symmetry and integer hole count (*n*). As a result, actual porosity (φ_{actual}) deviated slightly from the φ_{target}, with an average discrepancy of 0.31% and a maximum of 0.52%. Figure 1 presents a side view of the plug nozzle geometry. A hollow void within the plug, referred to here as the plug cavity, extends radially from the centerbody (CB) with radius (r_{CB}), shown in blue, to the underside of the internal porous cavity wall (r_{cav}).

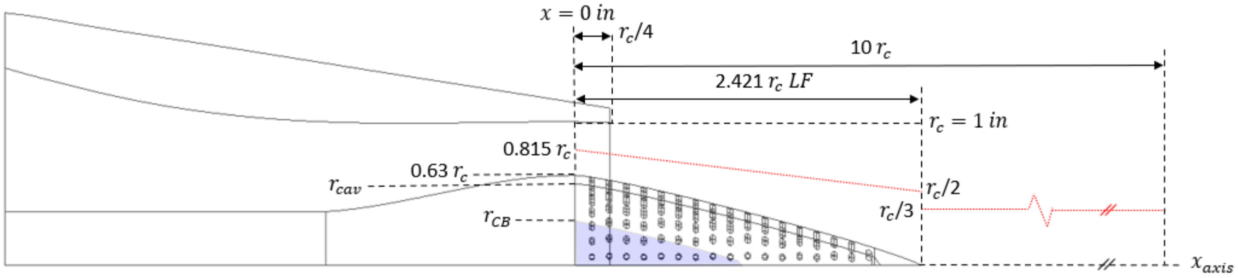

Figure. 1.: Side view of a sample porous plug nozzle geometry at experimental scale; s_{target} = 0.115 in., n = 82, r_{hole} = 0.0185 in., $\varphi_{actual} = 6.30\%$, with off-body (left) and downstream (right) CFD data extraction lines shown in red.

III. CFD Study of Parametric Sensitivities

A. Meshing

To enhance throughput and improve solution quality, the Sketch-to-Solution (S2S) framework [12] with automated meshing and Adaptive Mesh Refinement (AMR) via FUN3D was adopted. The S2S framework improves solution quality through the use of automated mesh adaptation, with highly stretched, feature-aligned tetrahedral cells for precise capture of the complex or discontinuous flow features as shown in Fig. 2. Moreover, it enables a fully automated CAD-to-solution workflow. The S2S framework inherently includes a mesh independence study for each case to confirm that variations across plug configurations are unaffected by continued mesh refinement. For the complex flows seen around porous plug nozzles, achieving full "mesh independence" is challenging, as continuous refinement, especially in AMR schemes, better approximates discontinuous and high-gradient features (e.g., shocks, turbulence, or boundary layer separation). Nonetheless, AMR typically outperforms fixed meshes of equivalent or much larger size in solution quality. A final mesh size of 372M cells was selected for all geometries under consideration, as key quantities stabilized at this level without notable changes in further refinement. Mesh sizes ranging from 45M to 1.48B cells were also evaluated, revealing local relative pressure ($P_{rel} = P/P_a - 1$) differences of less than 0.05% between the chosen 372M cell mesh and the next refinement level of 744M cells across the simulation domain. However, localized differences of up to 1% in flowfield quantities were observed near shock waves, caused by variations in shock resolution and alignment rather than substantial solution changes.

Recent findings by Galbraith et al. [13] suggest that for the Spalart-Allmaras turbulence model [14, 15], dimensionless wall distances (y^+) below 20 do not necessarily impact model accuracy when error-based mesh adaptation is applied. While the criterion $y^+ < 1$ is often used as one condition for reasonable accuracy, Galbraith et al. [13] argue that lower values do not always correlate strongly with numerical accuracy when using AMR, especially when boundary layer gradient resolution is sufficient off the wall. Accordingly, the appropriateness of any particular y^+ threshold depends on the model requirements and error tolerance of each application. For the S2S meshes in this study, a target y^+ of 5 was chosen as a balance between accuracy and computational cost, and smaller target y^+ values led to comparable discrepancies in flowfield quantities to those mentioned in the previous paragraph for increased refinement levels.

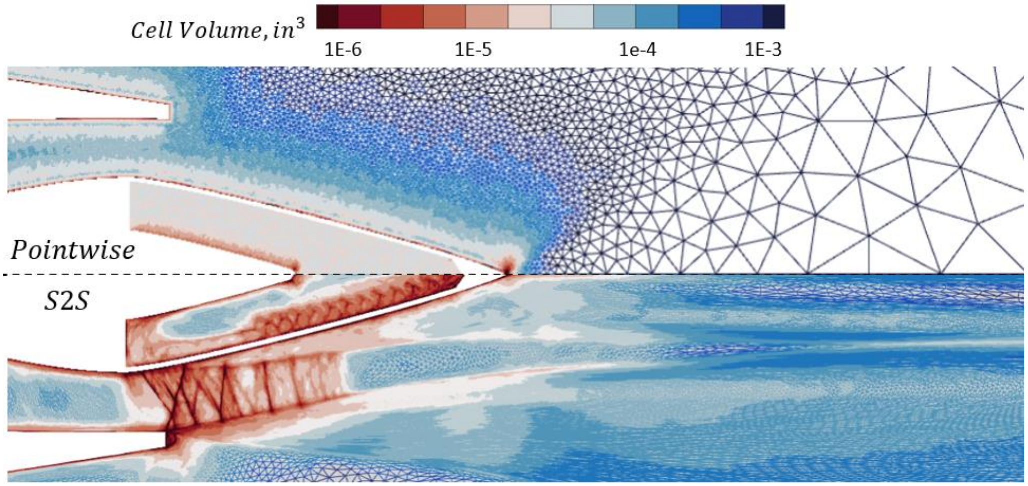

Figure 2. Meshes for a typical manually generated static 45M cell mesh (top) and Sketch-to-Solution adapted 372M cell mesh (bottom), colored by cell volume.

B. CFD Test Matrix and Simulation Methodology

Through the preliminary CFD studies, including nine cases for general design space exploration, it was determined that plug length factor (LF), target plug porosity (φ_{target}), and plug hole radius (r_{hole}) would be the independent variables of interest, while plug centerbody radius normalized by plug cavity inner wall radius (r_{CB}/r_{cav}) and plug wall thickness (w) would remain fixed at 0.5 and 0.04 in., respectively. A preliminary cavity volume study simulating r_{CB}/r_{cav} values of 0 (i.e., no centerbody), 0.5 and 0.8 found minimal impact on plug surface P_{rel} contours. P_{rel} deviations due to r_{CB}/r_{cav} were limited to a maximum of 1.54%. While both the medium-sized (r_{CB}/r_{cav}= 0.5) and no-centerbody configurations displayed nearly identical contours, the largest centerbody (i.e., the smallest cavity) caused a slight difference in P_{rel}. Similarly, a wall thickness study evaluating w values of 0.01 in., 0.04 in. and 0.08 in. showed a maximum deviation in plug surface P_{rel} contours of 2.1%, also at the jet separation point. Both findings suggest centerbody volume and wall thickness have limited influence on the pressure signature when evaluated on the combined extraction line (red lines in Fig.1). This supported the use of fixed values of r_{CB} and w in subsequent analysis.

The simulated ranges of the variables of interest are all permutations of LF values (0.7, 1.0, and 1.3), r_{hole} values (0.015 in., 0.0225 in., and 0.03 in.), and φ_{target} values (5%, 10%, and 15%), amounting to 27 unique geometries. An additional 3 solid plugs (0% porosity) and one porous plug with closed holes (i.e., without a cavity) were also simulated, bringing the total number of unique geometries to be simulated via FUN3D/S2S to 31, seen in Table 1. For each geometry, five CFD runs were performed at nozzle pressure ratios (NPR) corresponding to bulk jet Mach numbers (MJ) of 1.1, 1.2, 1.3, 1.4, and 1.5 [16]. All runs were performed with a static-to-total nozzle temperature ratio (NTR) of 1.68 with adiabatic walls. It should be noted that while the experimental NTR is effectively 1.00, a more flight-relevant NTR of 1.68 was chosen for consistency with past CFD efforts.

Table 1. Run matrix for porous plug nozzle CFD study.

$\boldsymbol{Case}$	$\boldsymbol{LF}$	$\boldsymbol{r_{hole}, in.}$	$\boldsymbol{\varphi_{target}}$	$\boldsymbol{\varphi_{actual}}$	$\boldsymbol{n}$
a.00	0.7	0	0.00%	0.00%	0
b.00	1	0	0.00%	0.00%	0
c.00	1.3	0	0.00%	0.00%	0
b.10.m.c	1	0.0225	0.00%	0.00%	91
a.05.s	0.7	0.015	5.00%	5.19%	72
b.05.s	1	0.015	5.00%	5.05%	100
c.05.s	1.3	0.015	5.00%	5.09%	131
a.10.s	0.7	0.015	10.00%	10.10%	140
b.10.s	1	0.015	10.00%	10.20%	202
c.10.s	1.3	0.015	10.00%	10.14%	261
a.15.s	0.7	0.015	15.00%	15.58%	216
b.15.s	1	0.015	15.00%	15.50%	307
c.15.s	1.3	0.015	15.00%	15.38%	396
a.05	0.7	0.0225	5.00%	5.36%	33
b.05	1	0.0225	5.00%	5.00%	44
c.05	1.3	0.0225	5.00%	5.16%	59
a.10	0.7	0.0225	10.00%	10.55%	65
b.10	1	0.0225	10.00%	10.34%	91
c.10	1.3	0.0225	10.00%	10.40%	119
a.15	0.7	0.0225	15.00%	14.77%	91
b.15	1	0.0225	15.00%	14.77%	130
c.15	1.3	0.0225	15.00%	15.38%	176
a.05.L	0.7	0.03	5.00%	5.48%	19
b.05.L	1	0.03	5.00%	5.66%	28
c.05.L	1.3	0.03	5.00%	5.13%	33
a.10.L	0.7	0.03	10.00%	11.26%	39
b.10.L	1	0.03	10.00%	10.50%	52
c.10.L	1.3	0.03	10.00%	10.26%	66
a.15.L	0.7	0.03	15.00%	15.01%	52
b.15.L	1	0.03	15.00%	16.16%	80
c.15.L	1.3	0.03	15.00%	15.54%	100

All FUN3D simulations were conducted assuming quarter-symmetry with the same meshing and refinement procedure via the S2S framework, with consistent farfield parameters: a flight Mach number of 0.1, unit Reynolds number of 5.34×10^4 /in., and freestream temperature of 72.9°F. The simulations were performed at a 25.4× scale relative to the experimental models presented in Section IV for possible relevance to future flight hardware. Experimental hardware has an internal cowl diameter of 2 in., correlating to a CFD internal cowl diameter of 50.8 in. Each simulation employed the improved one-equation Spalart-Allmaras turbulence model with negative handling [15], the Low-Diffusion Flux-Splitting Scheme [17] with a variant of the Van Leer flux limiter [18] for accuracy and stability, and the Hierarchical Adaptive Nonlinear Iterative Method (HANIM) non-linear solver [19] for speed and robustness. Initial volume meshes consisted of approximately 3×10^6 cells, which were refined via 22 mesh adaptations, culminating in 372×10^6 cells. The Mach number Hessian field, i.e. $\nabla^2 M$, was the adaptation metric used for the S2S mesh adaptations. At each mesh size, 500 sub-iteration steps were executed. To prevent adverse reactions near the farfield domain boundaries, artificial mesh coarsening was applied at 80% of the maximum farfield distance from the nozzle. Each simulation ran for 11,000 iterations, with convergence behavior matching prior S2S FUN3D cases. Flowfield similarities across 155 geometries made distinguishing trends difficult. To isolate the effects of key geometric changes, a summary of modifications and their impact precedes the analysis below of noise reduction mechanisms.

C. Effects of Hole Size

By investigating (experimental equivalent) hole radii of 0.015 in., 0.0225 in., and 0.03 in., the effect of hole size can be isolated and qualitatively assessed using simulated schlieren contour plots, which depict numerically obtained $\|\nabla\rho\|$. Figure 3 illustrates the effect of varying r_{hole} on the flow structures. For a fixed level of porosity, there is an inverse relationship between r_{hole} and n. It follows that, as n increases, the number of shocklets (alternatively termed barrier shocks, and defined here as a series of weak shocks propagating individually from the surface holes) from each row of holes increases, leading to more tightly-packed shocklets and smoother schlieren contours.

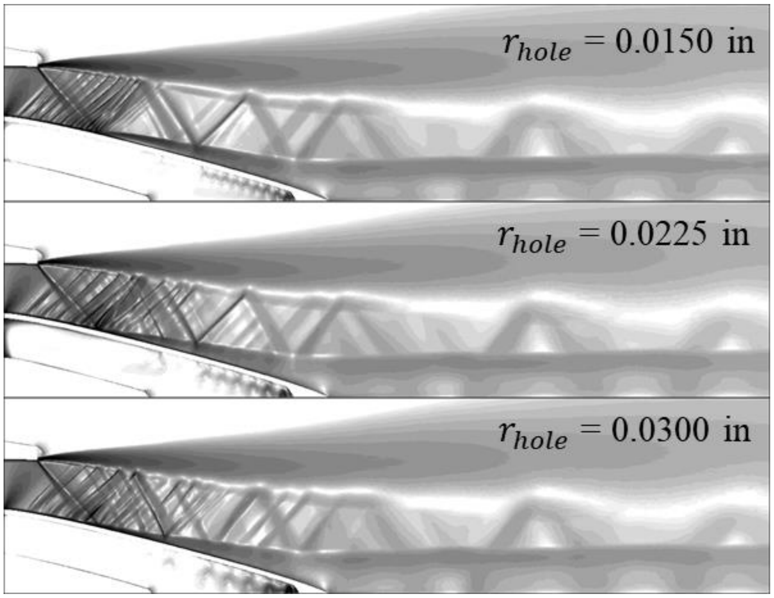

Figure 3. Simulated schlieren contour plot illustrating the effect of changing hole radius, LF = 1.0, φ_{target} = 10%, MJ =1.3.

Figure 4 shows relative pressure signals along the combined extraction line (red lines in Fig. 1) as hole size is varied on each plug length, with φ_{target} held constant at 10%. No meaningful variation is found in the figure between small (red), nominal (blue) and large holes (black) as hole size is varied, reinforcing the observation from the simulated schlieren images of similarity in downstream shock structures. Figure 5 shows radial mass flow through the holes, normalized by the peak outward mass flow attained in any of the 155 CFD runs. The negative and positive peaks denote flow into and out of the plug cavity, respectively. These results clearly show the nature of mass exchange between the cavity and the outer flow. Patterns of alternating inward and outward flow are observed in Fig. 5 to vary strongly as a function of jet Mach number. In contrast, because φ_{target} is held constant at 10%, there is a clear independence of hole mass flow to the hole pattern, number of holes, and hole radii.

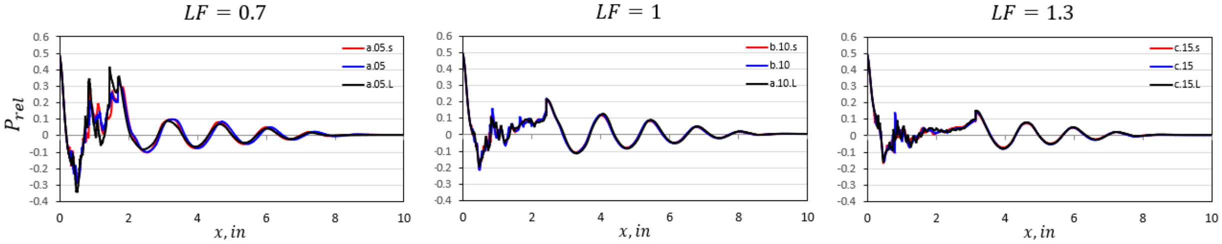

Figure 4. Relative pressure plots on the combined extraction line at MJ = 1.3, $\varphi_{target} = 5\%$ and LF = 0.7 (left), $\varphi_{target} = 10\%$ and LF = 1 (middle), $\varphi_{target} = 15\%$ and LF = 1.3 (right).

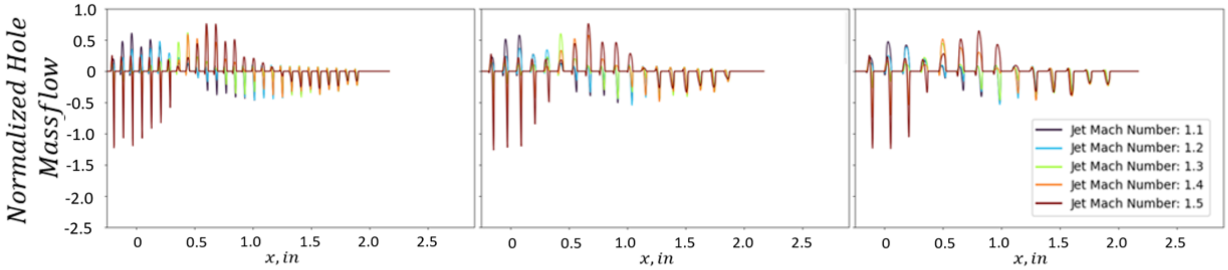

Figure 5. Normalized hole massflow for each hole radii; 0.015 in. (left), 0.0225 in. (middle), and 0.03 in. (right) for $\varphi_{\text{target}} = 10\%, LF = 1.3$.

The simulated schlieren contours show minimal qualitative changes across varying hole sizes. Clear groupings in the downstream relative pressure signals are observed by porosity, irrespective of hole size. Additionally, there is a pronounced similarity in mass flow characteristics through the holes for a given porosity and bulk jet Mach number. These observations together suggest that r_{hole} will have little if any effect on either shock patterns or BBSN.

D. Effects of Plug Length

Simulated schlieren plots are shown in Fig. 6 for three cases for which the plug length factor LF is varied, all with the same jet Mach number, porosity, and hole size. A key trend observed in the plots is that as LF increases, the internal jet shear layer, originating at the separation point on the plug surface, moves closer to the jet axis. In other words, a longer plug shifts the separation point downstream and toward the axis, narrowing the associated subsonic region. Some related differences in the pattern of reflected shocks between the internal jet shear layer and outer mixing layer are observed in Fig. 6, with potential consequences for downstream shock propagation and BBSN. Differences in reflected shock patterns are further illustrated in Fig. 7, where relative pressures along the combined extraction line are compared among the three length factors. Note that LF=0.7, 1.0 and 1.3 correspond to plug lengths of 1.695", 2.421" and 3.147", respectively. In all three plots, pressure is found to vary considerably with bulk jet Mach number *MJ*. A phase difference also occurs with varying *LF*, especially at *MJ*=1.3 and 1.5. The phase difference may be attributed to variation in the spacing between the internal shear layer and the outer mixing layer, which in turn alters the axial distance between reflected shocks.

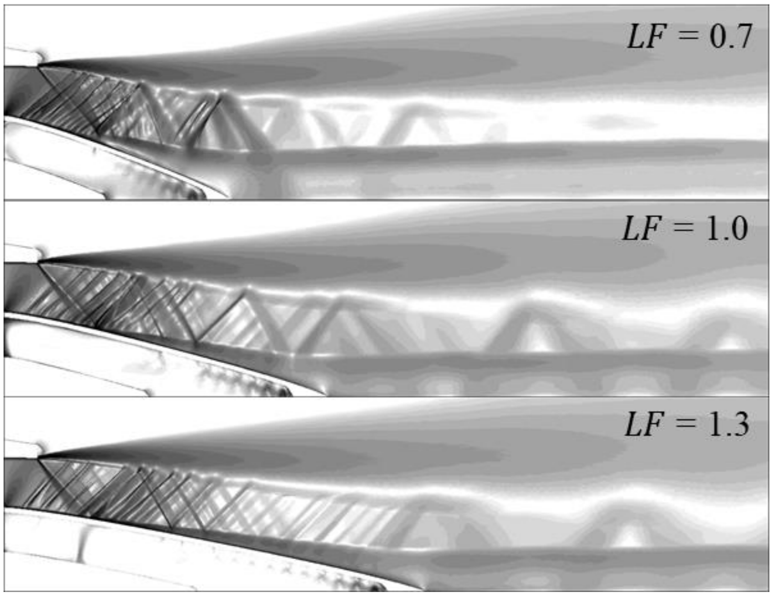

Figure 6. Simulated schlieren contour plot illustrating the effect of changing plug length factor, r_{hole} = 0.0225 in., φ_{target} = 10%, MJ = 1.3.

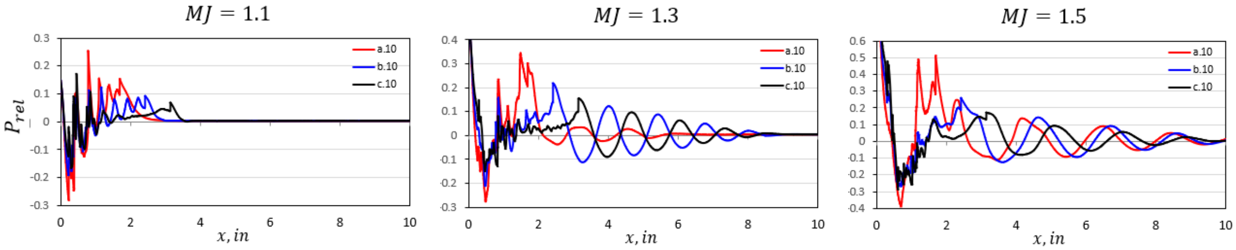

Figure 7. Relative pressure plots on the combined extraction line for MJ = 1.1 (left), MJ = 1.3 (middle), MJ = 1.5 (right), φ_{target} = 10%, r_{hole} = 0.0225 in.

Figure 8 shows normalized mass flow rates through the holes for the same geometries as in Fig. 6. Each of the three plots displays results for five MJ values indicated in the legend on the right. As in Fig. 5, upward and downward spikes denote inward and outward flow, respectively. Thus, at MJ = 1.5, primarily inward flow is seen near the upstream plug region, followed by a downstream reversal to outward flow, then a return to inward flow near the plug tip.

More generally, the characteristics of the mass flow through the holes is seen in Fig. 8 to be greatly affected by jet Mach number. At lower jet Mach numbers, the flow is primarily entering the plug holes near to the throat, and exiting near the plug tip. As the Mach number is increased, the flow has a greater tendency to enter the plug even closer to the throat, exit in the middle (where the primary expansion fan is impinging on the plug surface), and again enter the plug in the separation region downstream. Intermediate Mach numbers tend to smoothly blend those two behaviors, contrasting with a clear two zone, “in-out” behavior at MJ =1.1 and clear 3-zone “in-out-in” behavior at MJ =1.5, as illustrated in Fig. 8. These trends largely reflect pressure variations along the plug surface due to shock impingement and boundary layer separation. While trends in mass exchange tend to vary with MJ, these trends are found to have minimal qualitative dependence on LF, especially for the longer two cases.

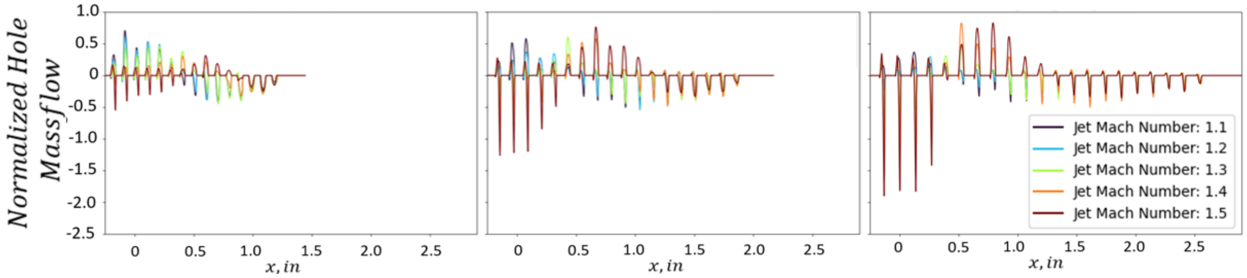

Figure 8. Normalized hole massflow for each plug length factor 0.7 (left), 1.0 (middle), and 1.3 (right), r_{hole} = 0.0225 in., φ_{target} = 10%.

E. Effects of Plug Porosity

Figure 9 presents simulated schlieren plots for *MJ*=1.3 and *LF*=1, with porosities ranging from 0% to 15%. As porosity increases, the separation point on the plug surface is observed in the figure to move upstream. This is thought to be due at least in part to a reduction in effectiveness of the Coanda effect [20] that would tend to keep the separated shear layer attached to the plug surface. The Coanda effect tends to promote attached flow and delayed boundary layer separation in the presence of an adverse pressure gradient, as is the case near the impingement location of the cowl lip shock. The effect is weakened by a porous surface due to outward flow (i.e., blowing) through the surface. With upstream movement of the separation point, the interior shear layer in the jet – which forms a boundary between the supersonic region containing shock diamonds and the partially subsonic region nearest to the plug tip – tends to move radially outward away from the axis. Another impact of increased porosity seen in Fig. 9, with potential relevance to BBSN, is a significant weakening of the shock diamonds downstream of the plug tip. This trend may be partly explained by the fact that, as the interior shear layer extends outward with increasing porosity, the jet in effect becomes less overexpanded, and weaker expansion fans are consequently formed at the intersection of outward-propagating oblique shocks and the edge of the subsonic mixing layer.

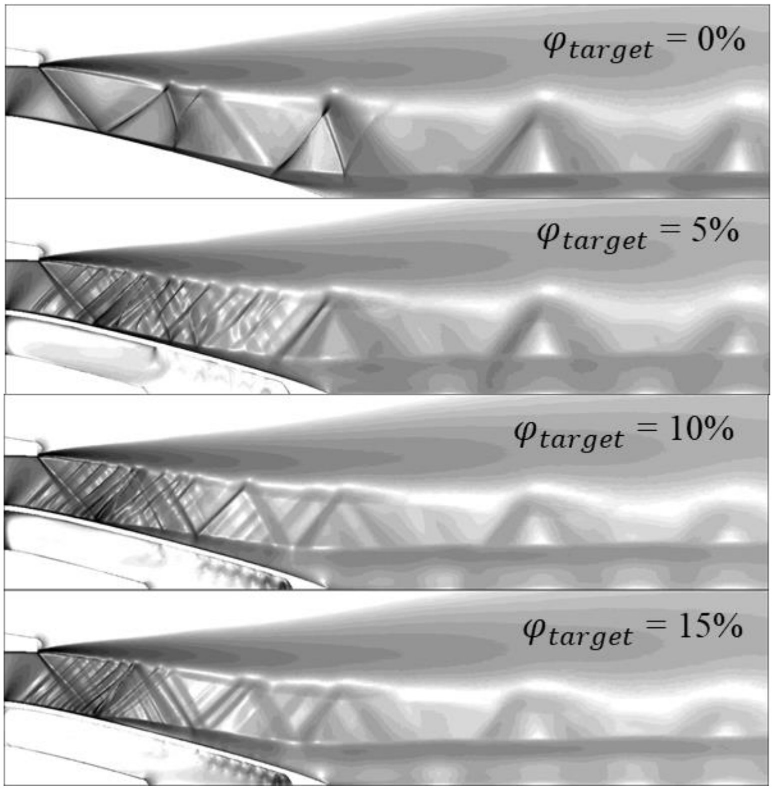

Figure 9. Simulated schlieren contour plot illustrating the effect of varying target plug porosity (φ_{target}), LF = 1.0, r_{hole} = 0.0225 in., MJ = 1.3.

The same tendency for reduced shock diamond strength with increasing porosity can be found in some – but not all – of the plots presented in Figures 10 through 12. Results for input parameter combinations (LF = 0.7, MJ = 1.1), (LF = 0.7, MJ = 1.3) and (LF = 1.3, MJ = 1.5) show an especially strong impact of porosity. Large pressure oscillations are found for the nonporous plug cases, whereas the oscillations are generally smaller for porous plugs. In a few cases, however, pressure oscillations are found to grow with increasing porosity. Such a counter-trend, as seen in the downstream region for the (LF = 1.3, MJ = 1.3) case, may be at least partially attributed to effects of constructive interference between the main reflected shocks and the weak compression waves (or shocklets) originating at individual holes along the plug surface. Note that the addition of porosity of 10% or higher effectively eliminates any shock diamonds aft of the plug tip for jet Mach numbers below 1.3 for the shortest plug (LF = 0.7), as observed in Figs. 10 (left) and 11 (left).

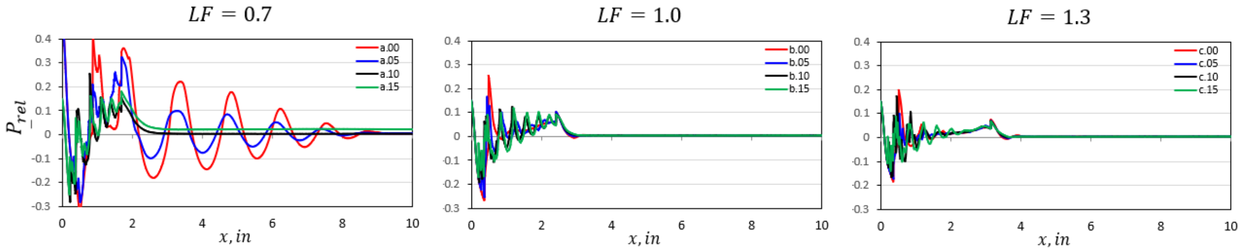

Figure 10. Effect of porosity on relative pressure on the combined extraction line for LF = 0.7 (left), LF = 1.0 (center) and LF = 1.3 (right), r_{hole} = 0.0225 in., MJ = 1.1.

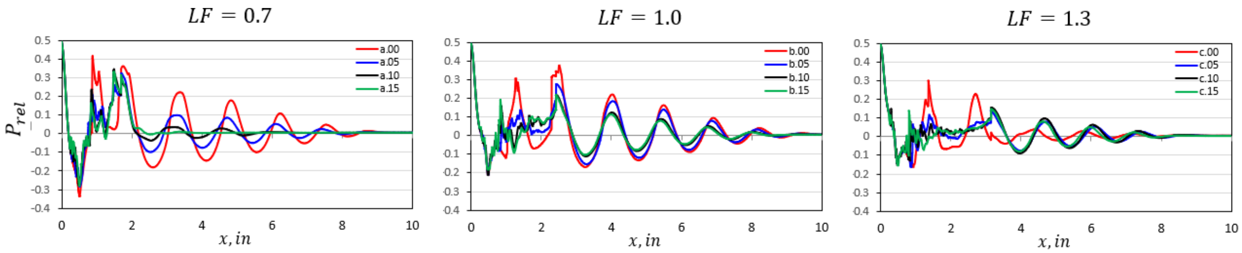

Figure 11. Effect of porosity on relative pressure on the combined extraction line for LF = 0.7 (left), LF = 1.0 (center) and LF = 1.3 (right), r_{hole} = 0.0225 in., MJ = 1.3.

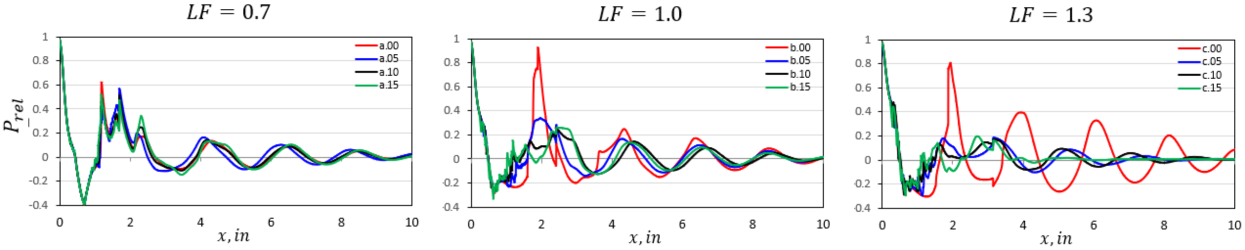

Figure 12. Effect of porosity on relative pressure on the combined extraction line for LF = 0.7 (left), LF = 1.0 (center) and LF = 1.3 (right), r_{hole} = 0.0225 in., MJ = 1.5.

F. Effects of Bulk Jet Mach Number

The influence of bulk jet Mach number MJ on the flowfields was found to be relatively complex, with some unique characteristics observed at specific Mach numbers for each LF value. Simulations were conducted for MJ values ranging from 1.1 to 1.5, in increments of 0.1, with corresponding nozzle pressure ratios (NPR) of 2.13, 2.43, 2.77, 3.18 and 3.67. Across the 31 nozzle configurations examined, several consistent trends in overall flowfield characteristics emerged with increasing Mach number. Simulated schlieren contour plots at various jet Mach numbers for configuration b.10 are shown in Fig. 13, and the associated relative pressure signals along the combined extraction line are shown in Figs. 14 through 17. As expected, the average angle of both primary shocks and shocklets from the holes increased with Mach number, correlating with stronger individual shocks, while the expansion fan from the cowl lip corner grew in angular width and strength. A distinct separation region formed where the aft end of the cowl lip expansion fan intersected the plug surface. As a consequence of this separation, the forward movement of the separation point on the plug with increasing Mach number led to a reduction in the downstream jet width, affecting both the phase and strength of the shock reflections off the inner and outer shear layers. The strength of the shock diamonds generally increased with Mach number, particularly for non-porous plugs; however, exceptions were observed in cases such as high-porosity and long-length plugs (e.g., configuration c.15). In the latter cases, the weakest shock diamonds occurred at the highest Mach number. These findings highlight the complex nature of plug nozzle flowfields under varying jet Mach numbers.

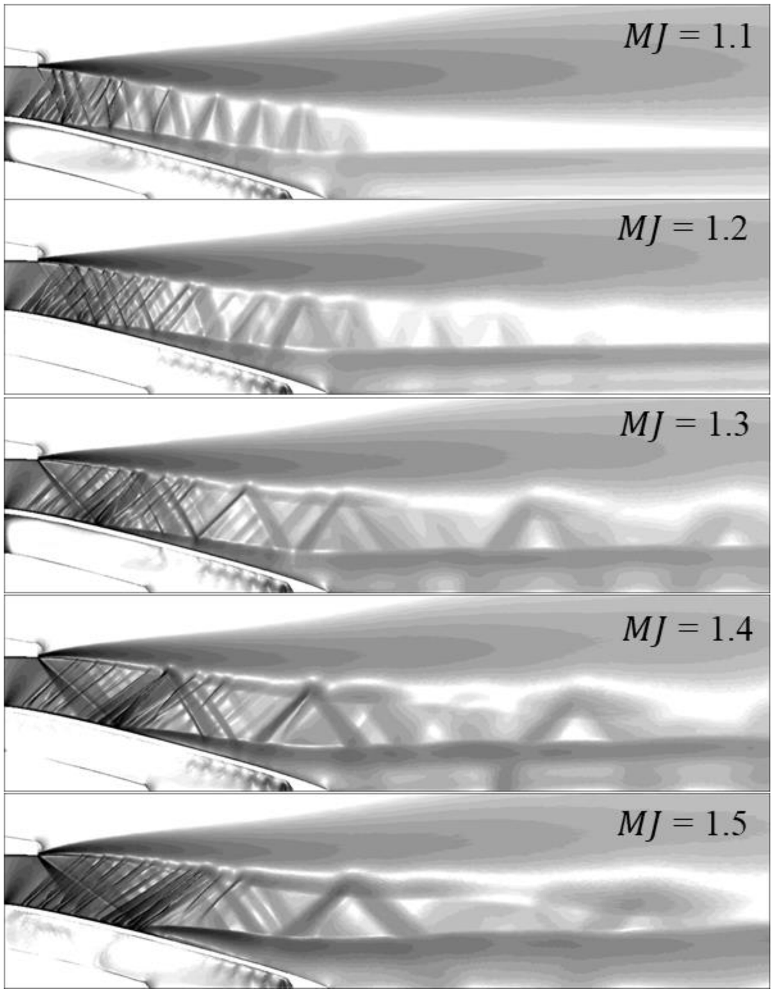

Figure 13. Simulated schlieren contour plot illustrating the effect of changing bulk jet Mach number MJ, with LF =1.0, φ_{target} = 10%, r_{hole} = 0.0225 in.

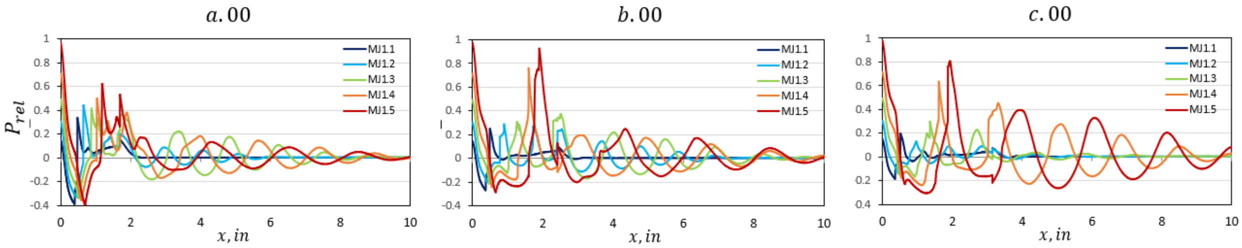

Figure 14. Effect of jet Mach number on relative pressure on the combined extraction line for LF = 0.7 (left), LF = 1.0 (middle) and LF = 1.3 (right), r_{hole} = 0.0225 in., φ_{target} = 0%.

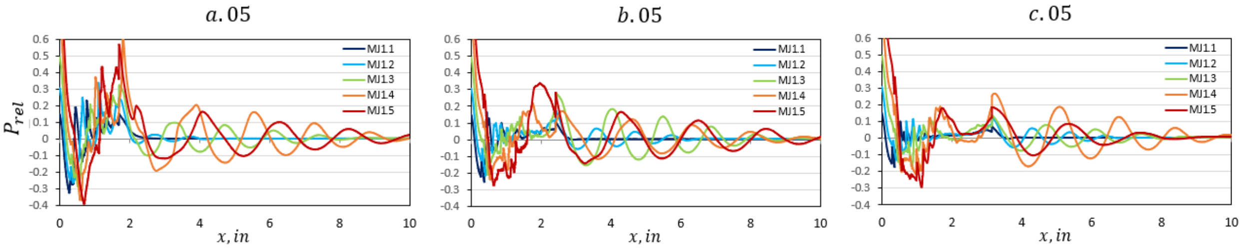

Figure 15. Effect of jet Mach number on relative pressure on the combined extraction line for LF = 0.7 (left), LF = 1.0 (middle) and LF = 1.3 (right), r_{hole} = 0.0225 in., φ_{target} = 5%.

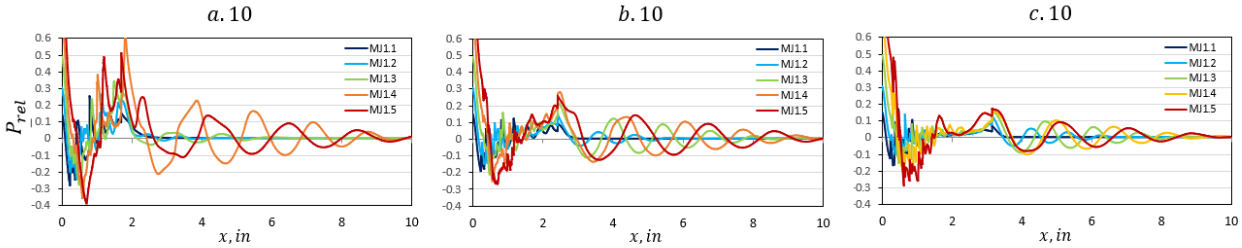

Figure 16. Effect of jet Mach number on relative pressure on the combined extraction line for LF = 0.7 (left), LF = 1.0 (middle) and LF = 1.3 (right), r_{hole} = 0.0225 in., φ_{target} = 10%.

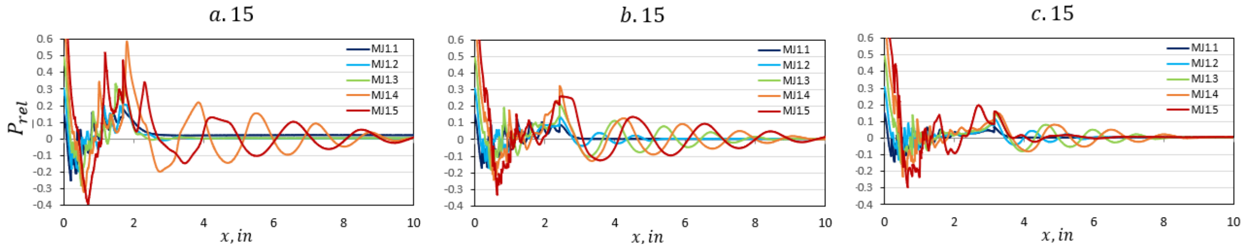

Figure 17. Effect of jet Mach number on relative pressure on the combined extraction line for LF = 0.7 (left), LF = 1.0 (middle) and LF = 1.3 (right), r_{hole} = 0.0225 in., φ_{target} = 15%.

A RANS-based metric (ζ_{BBSN}) for shock-diamond strength, presented in Eq. 1, may be computed by integrating the square of the pressure over the combined extraction line. This metric is shown graphically in Fig. 18 for all medium hole size (**r_{hole} = 0.0225 in**) cases. Stronger shocks are presumed to produce increased shock-associated noise, as demonstrated by Zaman et al. [6]. Thus, a larger value of this metric, particularly in the jet's downstream region, is expected to result in elevated BBSN levels. A comparative analysis of the short plug cases for $MJ = 1.3$ reveals a distinct correlation between ζ_{BBSN} and the strength of shock diamonds downstream of the plug. Specifically, the a.00 case exhibits the highest ζ_{BBSN}, whereas values for both a.10 and a.15 are relatively low. The a.05 case occupies an intermediate position, with the trend reversing around MJ =1.4. This observation aligns closely with noise data from [6], suggesting a direct link between shock diamond intensity (ζ_{BBSN}) and noise. This effect is most pronounced in the intermediate MJ range of 1.2-1.4, consistent with observations by Zaman et al. [6] of "*... a dramatic reduction in shock strength for the porous case in the mid-MJ range*". To elucidate noise reduction mechanisms, two extreme cases of porosity-induced ζ_{BBSN} reduction – a.00 vs a.10 and c.00 vs c.10 – were analyzed.

$$\zeta_{BBSN} = \int_{X_{tip}+r_c}^{X_{tip}+10r_c} {P_{rel}}^2 dx \tag{1}$$

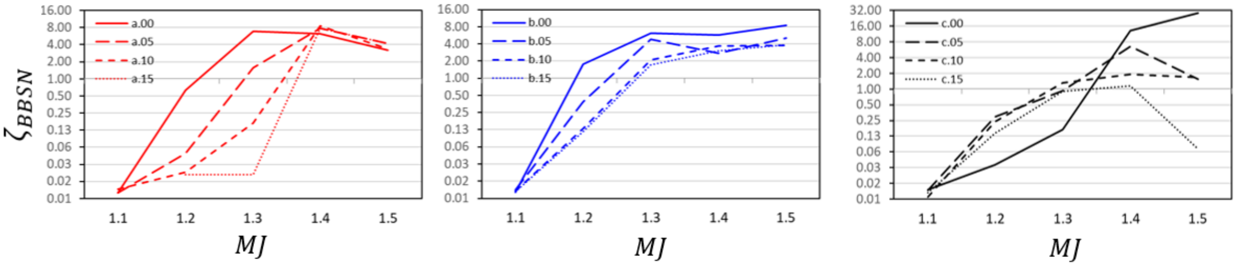

Figure 18. X-integral of the combined relative pressure signals from 1 to 10 in. aft of the plug tip, for *LF* = 0.7 (left), *LF* = 1.0 (middle) and *LF* = 1.3 (right).

IV. Experimental Results and Comparison to CFD

A. Experimental Setup

The experiments were conducted in the open-jet CW-17 facility at NASA Glenn Research Center. The experimental arrangement, shown in Fig. 19 (set up for thrust measurement), was utilized to acquire both noise data and schlieren images. Flow from the main plenum chamber was directed through four U-shaped tubes to a 5 in. diameter ‘floating plenum’ mounted on a linear bearing, allowing axial thrust measurements. A plug nozzle was attached to the downstream end of the floating plenum, featuring a cowl with a 2 in. exit diameter. A screw mechanism, supported centrally within the nozzle by x-shaped struts, was used to attach interchangeable plugs. Sound pressure spectrum data were obtained using overhead microphones. Further details of the configuration are available in previous publications [9].

Figure 19. Experimental setup of the CW-17 open jet facility.

A focusing schlieren system with a lens-and-grid technique was used for flow visualization, projecting a source grid onto a retro-reflective screen and imaging it onto a cut-off grid to produce the schlieren effect, as detailed in [21]. A 5-watt xenon flashlamp with a 1-microsecond pulse illuminated the flow. Density gradients cause light rays to refract, and by using a cut-off grid similar to the "knife-edge" in classical schlieren systems, these disturbances are visualized as light and dark regions in images captured by a scientific-grade CCD camera. Optical components and the camera were enclosed in a light-tight box on one side of the jet, with a 30 in. x 24 in. retro-reflective screen on the opposite side, providing a 10 in. field of view along the streamwise direction and 3.5 in. vertically around the jet centerline. The camera captured 30 images at 3 frames per second, averaging them over a 10-second period. Background subtraction and contrast enhancement were performed during post-processing to improve the image quality. Figure 20 shows a schematic of the system.

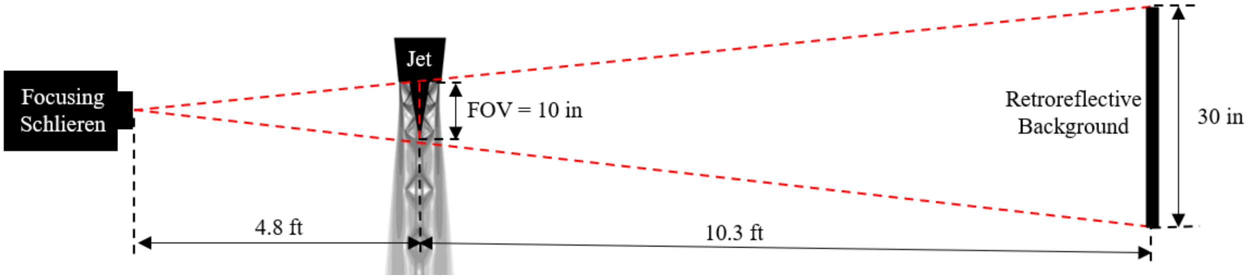

Figure 20. Overhead view schematic of the focusing schlieren layout in the CW-17 free-jet facility.

The focal plane of the schlieren system spanned about 2 in. This setup caused measurements to be a ray-integrated representation of ∂ρ/∂x across the focal length, contrasting with the CFD-extracted, infinitesimally thin plane used in simulated schlieren images. This thin plane, extracted from the volume solution, provides higher resolution of local flow features but limits direct comparability, as illustrated in Fig. 21. Furthermore, experimental images are time-averaged and are affected by shock oscillations, turbulence, and measurement noise, while CFD yields instantaneous simulated schlieren contours. In spite of these differences, experimental and simulated schlieren images show good overall agreement, as is evident from Fig. 21.

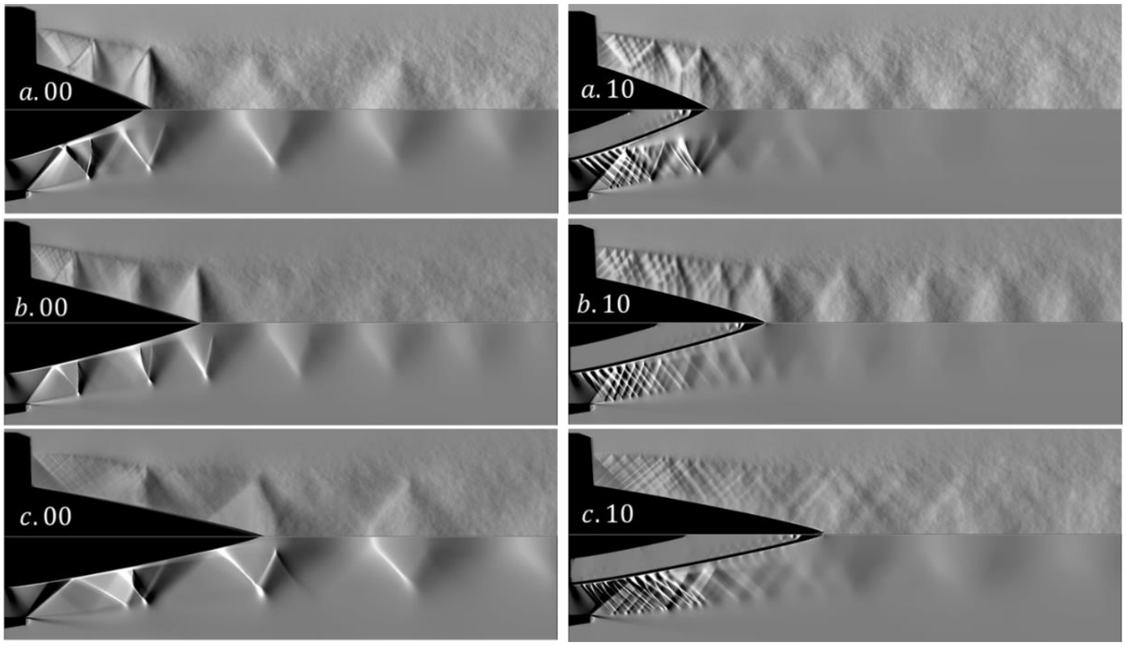

Figure 21. Comparison of experimental (top) and simulated schlieren (bottom) images for short, medium, and long plugs (top to bottom), with non-porous (left) and φ_{target} = 10% (right) configurations.

B. Noise Data

Noise data was taken across all experimental geometries for MJ =1.2, MJ =1.3 and MJ =1.4, as the largest differences in porosity-induced relative pressure signals were seen at those Mach numbers computationally.

The data for all relevant test configurations, namely a.00 through a.15, b.00 through b.15, and c.00 through c.15, can be seen below in Figs. 22 through 24.

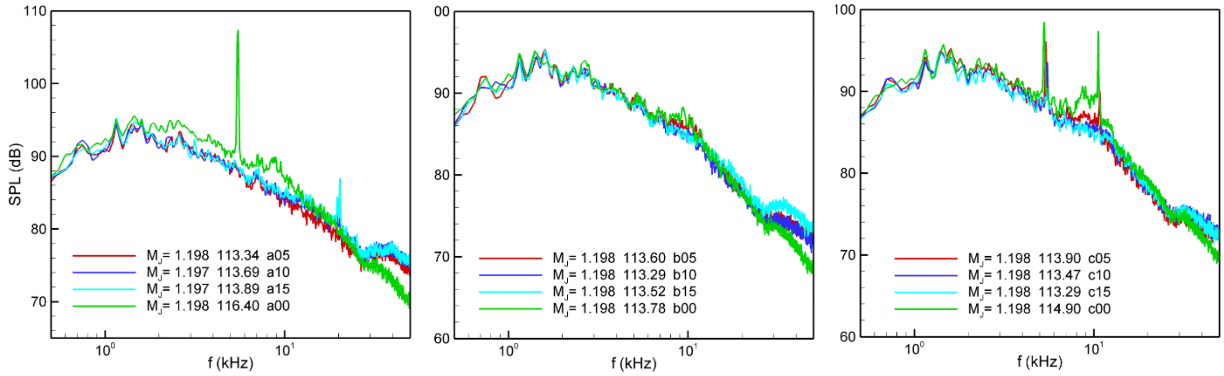

Figure 22. Noise spectra for non-porous (green), φ_{target} = 5% (red), φ_{target} = 10% (blue) and φ_{target} = 15% (cyan), for LF = 0.7 (left), LF = 1.0 (middle) and LF = 1.3 (right), at MJ = 1.2.

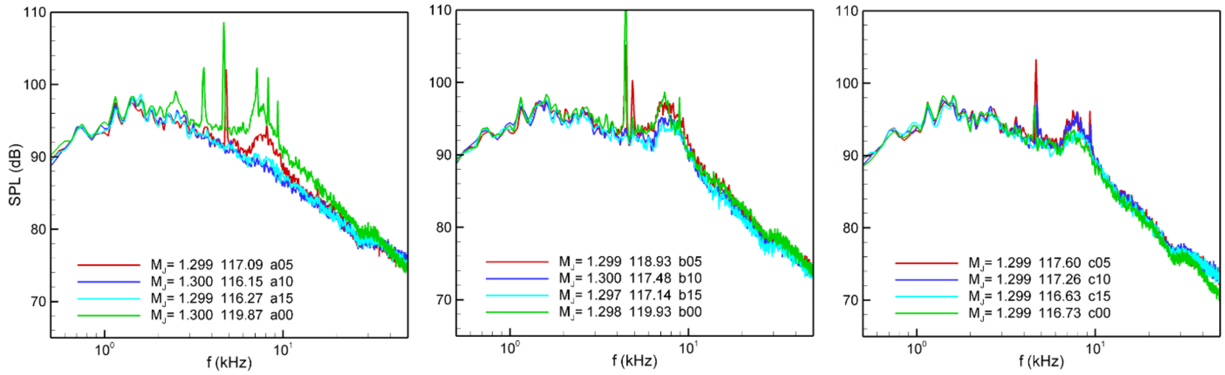

Figure 23. Noise spectra for non-porous (green), φ_{target} = 5% (red), φ_{target} = 10% (blue) and φ_{target} = 15% (cyan), for LF = 0.7 (left), LF = 1.0 (middle) and LF = 1.3 (right), at MJ = 1.3.

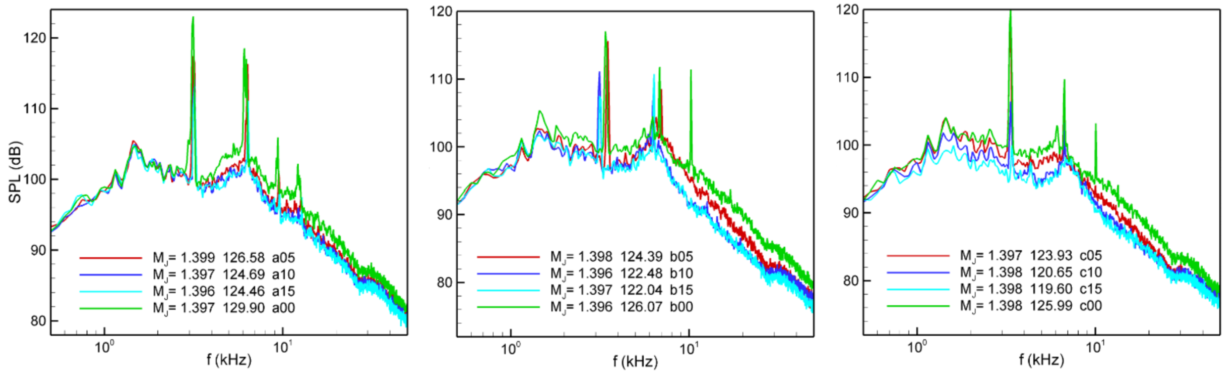

Figure 24. Noise spectra for non-porous (green), φ_{target} = 5% (red), φ_{target} = 10% (blue) and φ_{target} = 15% (cyan), for LF = 0.7 (left), LF = 1.0 (middle) and LF = 1.3 (right), at MJ = 1.4.

A conclusion from the noise spectra is that at lower jet Mach numbers (e.g., MJ =1.2 in Fig. 22), reductions in broadband shock noise at mid-frequencies due to plug porosity are often accompanied by a corresponding increase in high-frequency broadband noise. The high frequency noise is apparently due to the contribution of shocklets from the holes. This high frequency noise may present challenges to perceived human annoyance levels in scaled-up configurations. Adopting smaller sized holes might alleviate this concern, but further study is needed before any such design recommendations can be made.

V. Possible Mechanisms for Jet Noise Reduction

As described in Subsection III.E, increasing plug porosity can significantly reduce the strength and persistence of shock diamonds, thereby reducing BBSN. However, the effects are sensitive to various factors, such as the jet Mach number and plug shape. No single physical mechanism is sufficient to fully explain the observed trends, but a partial explanation may be inferred from certain cases, illustrated in Figs. 25 through 28, where the impact of porosity is especially favorable. In these cases, porosity causes a clear weakening or even elimination of shock diamonds within a short distance of the plug tip. One plausible explanation for this trend is that for a non-porous plug (φ_{target} = 0%), the Coanda effect typically prevents or reduces boundary layer separation around shock reflection points on the plug surface. A porous plug surface reduces the effectiveness of the Coanda effect because flow through the surface counters the radially inward forcing due to mixing layer entrainment, diminishing the plug's ability to resist boundary layer separation. As porosity increases, the separated region grows and moves upstream, causing a radially outward displacement of the separation-induced free shear layer within the jet. Such outward displacement in turn constricts the adjacent jet region containing shock diamonds, effectively reducing the degree of overexpansion within the jet. As overexpansion decreases – specifically, as the pressure variation across the inward-directed expansion fans at the junction of oblique shocks and the mixing layer edge is reduced – the shock diamond pattern becomes unable to persist far downstream. This explanation is consistent with observations in the cases shown in Figs. 25 through 28.

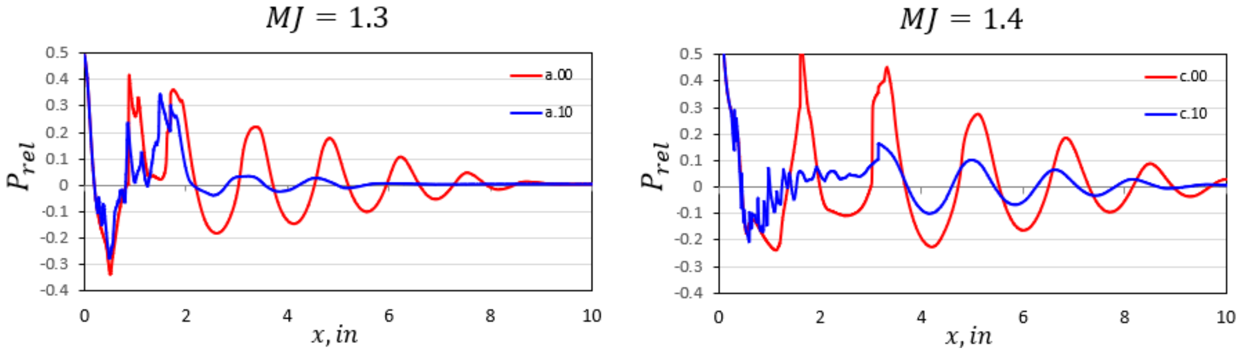
MJ = 1.3

MJ = 1.4

Figure 25. Relative pressure signals for the combined extraction line for cases a.00 vs a.10 at MJ = 1.3 (left) and c.00 vs c.10 at MJ = 1.4 (right).

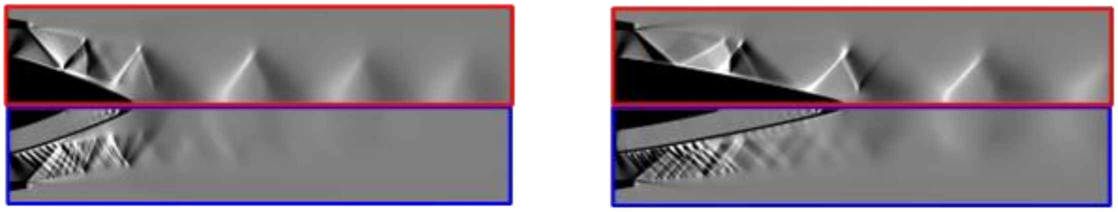

Figure 26. Simulated schlieren contour plots for a.00 (red) vs a.10 (blue) at MJ = 1.3 (left), c.00 (red) vs c.10 (blue) at MJ = 1.4 (right).

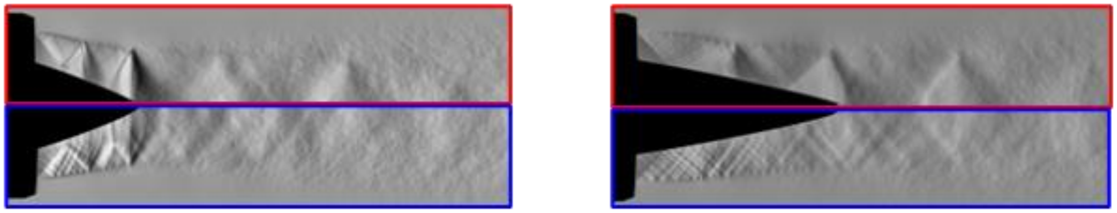

Figure 27. Experimental schlieren images for a.00 (red) vs a.10 (blue) at MJ = 1.3 (left), c.00 (red) vs c.10 (blue) at MJ = 1.4 (right).

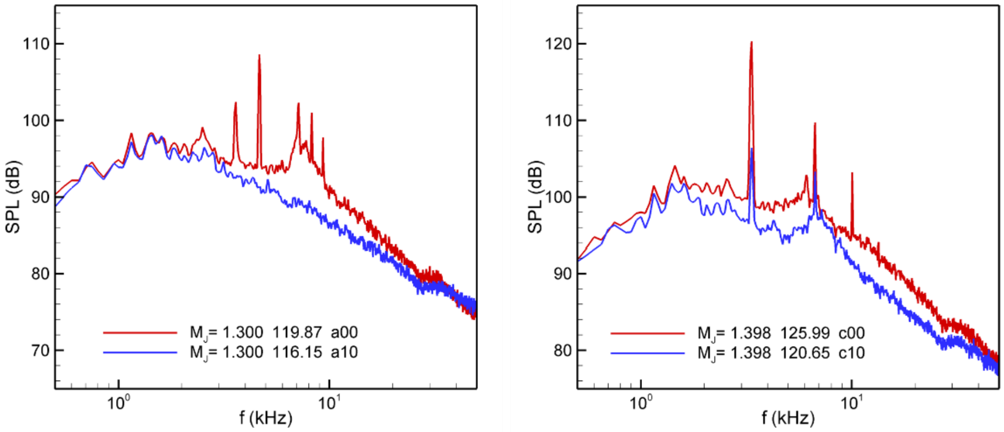

Figure 28. Noise spectra for a.00 (red) vs a.10 (blue) at MJ = 1.3 (left), c.00 (red) vs c.10 (blue) at MJ = 1.4 (right).

In other cases, the effect of plug porosity on shock diamond persistence is less favorable. In fact, in certain instances, shock diamonds tend to be stronger for a porous plug than for an equivalent nonporous plug; see for example a.00 vs a.10 for MJ =1.4 and c.00 vs c.15 for MJ =1.3 in Figs. 29 through 32. Notably, these two cases, chosen for their minimal or adverse effect on shock diamond strength, are adjacent in the case matrix to the two most favorable cases discussed in Figs. 25 through 28, seen in Table 1. This indicates that the design choices that significantly reduce BBSN via the advantageous effects of plug porosity may have no effect, or even adverse effects, at porosity values just slightly off the "design" condition. Further confirmation of this reversal in porosity effects on shock diamond strength can be seen in Fig. 18 (subsection III.F) as a crossing of lines representing 0% and 10% porosity between MJ =1.3 and MJ =1.4, as is observed for both the short (**LF = 0.7)** and long (**LF = 1.3**) plugs.

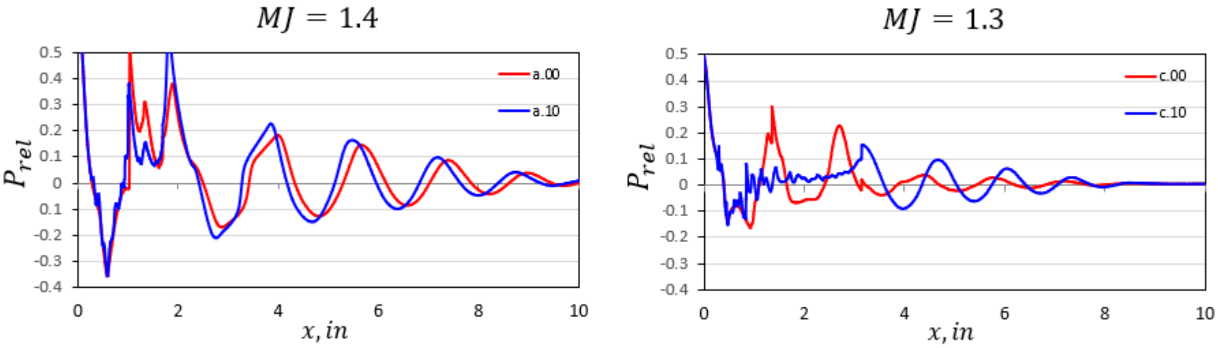

Figure 29. Relative pressure signals for the combined extraction line for cases a.00 vs a.10 at MJ = 1.4 (left) and c.00 vs c.10 at MJ = 1.3 (right).

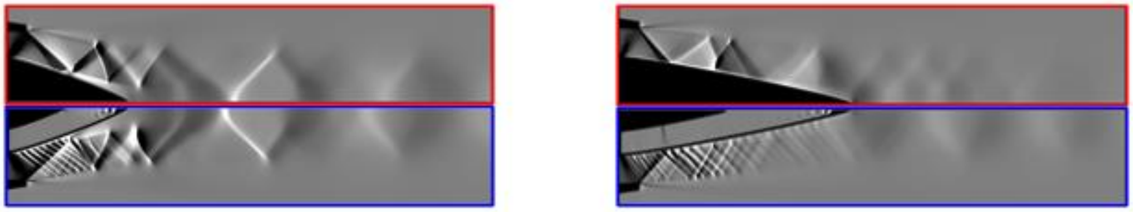

Figure 30. Simulated schlieren contour plots for a.00 (red) vs a.10 (blue) at MJ = 1.4 (left), c.00 (red) vs c.10 (blue) at MJ = 1.3 (right).

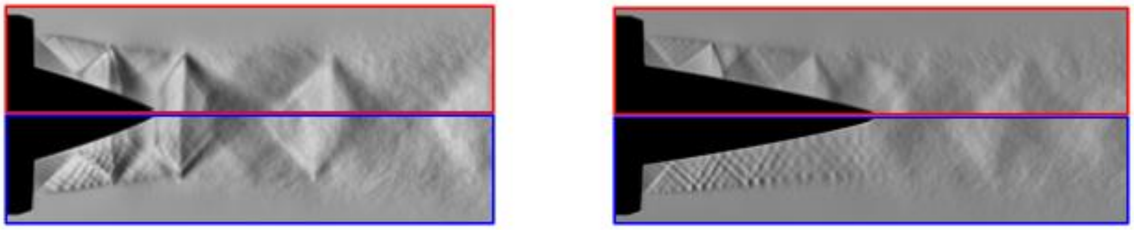

Figure 31. Experimental schlieren images for a.00 (red) vs a.10 (blue) at MJ = 1.4 (left), c.00 (red) vs c.10 (blue) at MJ = 1.3 (right).

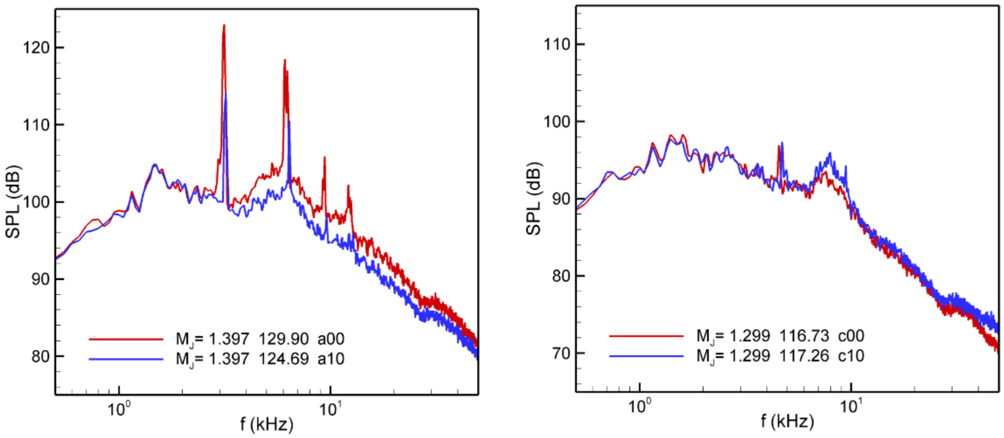

Figure 32. Noise spectra for a.00 (red) vs a.10 (blue) at MJ = 1.4 (left), c.00 (red) vs c.10 (blue) at MJ = 1.3 (right).

The reversal of porosity-induced effects on the shock diamonds – from advantageous to adverse as MJ is increased – may be explained partially by variation with MJ in the relative impact of competing effects. For example, shock-shock interactions may lead to either constructive or destructive interference, strengthening or weakening the primary shock reflections [22]. More specifically, weak shocklets generated from individual holes interact both with one another and with reflections from the cowl lip shock, potentially leading to constructive interference that amplifies shock strength and local flow disturbances. This interaction can lead to increased complexity in the shock structure, as overlapping shock waves merge, reinforcing each other and creating a more prominent, high-pressure shock front. With increasing jet Mach number, these interactions become more frequent and intense, steepening pressure gradients and amplifying shock-boundary layer interactions and downstream flow effects. Additional complexity arises from the recompression shock forming at the plug tip, and from the transmission and attenuation of shocks through the separation-induced shear layer.

VI. Conclusions

This study investigates the potential of porous plug nozzles to reduce landing and takeoff (LTO) noise for prospective commercial supersonic aircraft employing low-bypass turbofan engines. Building on previous experiments, this study expands in scope to various geometric configurations and employs Reynolds-averaged Navier-Stokes (RANS) computational fluid dynamics (CFD) simulations to examine 31 porous plug nozzle designs across jet Mach numbers from 1.1 to 1.5. An automated mesh refinement (AMR) technique is shown to provide excellent resolution of complex and/or discontinuous flow features. The CFD results, combined with experimental testing of 15 subscale nozzles, reveal multiple noise reduction mechanisms.

The primary mechanism at low supersonic jet Mach numbers, particularly relevant to LTO conditions, is a diminished Coanda effect with increased porosity. This results in an expanding jet that has less tendency to adhere to the plug surface, effectively behaving as a less overexpanded jet. A secondary mechanism, induced by the primary effect, involves the destructive interference between porosity-induced shocklets and primary shock structures. As the Coanda effect weakens and the separation point shifts upstream, the radial extent of the internal shear layer increases, narrowing the annular jet core width. This shift alters the phase and relative strength of the shocks, enabling stronger shocks to traverse the internal shear layer while weaker shocks reflect back into the jet. A resulting increase in shock interactions may then facilitate beneficial destructive interference between shocks and expansion fan structures.

Other noise characteristics of shocks in supersonic jets seem to diminish or negate the effects of plug porosity as the Mach number increases, in a trend exacerbated by shorter plug lengths. Further research is necessary to determine the relative impact and magnitude of these isolated effects, as well as to identify mechanisms that can be optimized at LTO-relevant conditions to mitigate the community noise impact of commercial supersonic transport. Although RANS provides some insights into broad band shock-associated noise (BBSN) levels, a direct correlation between RANS indicators and jet noise levels remains unestablished. Existing RANS-based noise prediction methods for BBSN are primarily limited to free jets without nearby surfaces. Nonetheless, these methods could be adapted to predict noise changes resulting from modifications in shock cell persistence downstream of the plug, such as those influenced by porosity. Future research should focus on optimizing flight-weight porous plug nozzle designs, enhancing correlations between high-fidelity RANS CFD solutions and experimental noise measurements, isolating noise reduction mechanisms, and conducting studies at lower jet Mach values (e.g., for MJ within the range 0.9 to 1.1). Further advances are also needed in plug nozzle design optimization for LTO noise, with utilization of higher-fidelity noise measurements and tailored experimental testing.

VII. Acknowledgements

Support for this work was provided by the NASA Commercial Supersonic Technology (CST) project. The authors extend their thanks to several individuals at NASA Glenn Research Center, including James Bridges, Stewart Leib, Will Banks, Julie Dudek and Evan McFadden. Special thanks also go to Bil Kleb and Lori Ozoroski at NASA Langley Research Center.

VIII. References

[1] Rowe, W. T., Johnson, E. S., and McKinnon, R. A., "Technology Status of Jet Noise Suppression Concepts for Advanced Supersonic Transports," *Journal of Aircraft*, Vol. 16, No. 2, 1979, pp. 95-101.

[2] Bridges, J., Stephens, D. B., and Berton, J. J., "Quantifying Uncertainty of Landing and Takeoff Noise for Commercial Supersonic Aircraft", *AIAA Paper* 2022-3051, 28th AIAA/CEAS Aeroacoustics Conference, June 14-17, 2022. DOI: 10.2514/6.2022-3051.

[3] Berton, J. J., “Variable Noise Reduction Systems for a Notional Supersonic Business Jet”, *Journal of Aircraft*, Vol. 60, No. 3, 2023, pp. 688-701. DOI: 10.2514/6.2022-2489.

[4] Sadeghian, M., and Bandpy, M. G., “Technologies for Aircraft Noise Reduction: A Review,” *Journal of Aeronautics & Aerospace Engineering*, Vol. 9, No. 219, 2020, pp. 1-10. DOI: 10.35248/2168-9792.20.9.219.

[5] Zaman, K. B. M. Q., Bridges, J. E., Castner, R. S., and Fagan, A. F., “An Investigation of Mixer-Ejector Nozzles for Jet Noise Reduction,” *AIAA Paper* 2019-2494, 25th AIAA/CEAS Aeroacoustics Conference, May 20-23, 2019. DOI: 10.2514/6.2019-2494.

[6] Zaman, K. B. M. Q., Fagan, A. F., Bridges, J. E., and Heberling, B. C., “Flow and Noise from Supersonic Plug Nozzles,” *AIAA Paper* 2022-2828, 28th AIAA/CEAS Aeroacoustics Conference, June 14-17, 2022. DOI: 10.2514/6.2022-2828.

[7] Zaman, K. B. M. Q., and Heberling, B. C., “A Study of Flow and Noise from Supersonic Plug Nozzles,” *AIAA Paper* 2021-2304, AIAA Aviation Forum, August 2-6, 2021. DOI: 10.2514/6.2021-2304.

[8] Korth, J. H., “Optimization of Plug Nozzles Using CFD Informed Design Space Querying,” *AIAA Paper* 2024-1776, AIAA SciTech Forum, January 8-12, 2024. DOI: 10.2514/6.2024-1776.

[9] Zaman, K. B. M. Q., Fagan, A. F., and Korth, J. H., “Flow, Noise and Thrust of Supersonic Plug Nozzles,” *AIAA Paper* 2024-2305, AIAA SciTech Forum, January 8-12, 2024. DOI: 10.2514/6.2024-2305.

[10] Biedron, R. T., Carlson, J.-R., Derlaga, J. M., Gnoffo, P. A., et al., “FUN3D Manual, Version 13.7,” *NASA Technical Memorandum*, NASA/TM- 20205010139, 2020.

[12] Kleb, W. L., Park, M. A., Wood, W. A., Bibb, K. L., Thompson, K. B., and Gomez, R. J., “Sketch-to-Solution: An Exploration of Viscous CFD with Automatic Grids,” *AIAA Paper* 2019-2948, AIAA Aviation Forum, June 17-21, 2019. DOI: 10.2514/6.2019-2948.

[13] Galbraith, M. C., Ursachi, C.-I., Chandel, D., Allmaras, S. R., Darmofal, D. L., Glasby, R. S., Stefanski, D. L., Erwin, J. T., Holst, K. R., Hereth, E. A., Mukhopadhaya, J., Alonso, J. J., and Diskin, B., “Mesh Convergence of RANS Solutions Using Expert Crafted and Output-Based Adapted Meshes,” Massachusetts Institute of Technology Aerospace Computational Design Laboratory Seminar Series, September 30, 2022.

[14] Deck, S., Duveau, P., d’Espiney, P., and Guillen, P. “Development and Application of Spalart–Allmaras One Equation Turbulence Model to Three-Dimensional Supersonic Complex Configurations,” *Aerospace Science and Technology*, Vol. 6, Issue 3, 2002, pp. 171-183. DOI: 10.1016/S1270-9638(02)01148-3.

[15] Anderson, W. K., Wood, S. L., and Allmaras, S. R., “An Initial Exploration of Improved Numerics within the Guidelines of the Negative Spalart-Allmaras Turbulence Model,” *NASA Technical Memorandum*, NASA/TM–2019–220429, 2019.

[16] Ames Research Staff, “Equations, Tables, and Charts for Compressible Flow,” *NACA Report* 1135, 1953.

[17] Edwards, J. R., “A Low-Diffusion Flux-Splitting Scheme for Navier-Stokes Calculations,” *Computers and Fluids*, Vol. 26, Issue 6, 1997, pp. 635-659. DOI: 10.1016/S0045-7930(97)00014-5.

[18] Liou, M.-S., Van Leer, B., and Shuen, J.-S., “Splitting of Inviscid Fluxes for Real Gases,” *Journal of Computational Physics*, Vol. 87, Issue 1, 1990, pp. 1-24. DOI: 10.1016/0021-9991(90)90222-M.

[19] Dacles-Mariani, J., and Liu, Y., “Assessment of Preconditioner for a USM3D Hierarchical Adaptive Nonlinear Iteration Method (HANIM),” *AIAA Paper* 2016-0860, 54th AIAA Aerospace Sciences Meeting, January 4-8, 2016. DOI: 10.2514/6.2016-0860.

[20] Cîrciu, I., and Rotaru, C., “Theoretical and Practical Aspects of the Coandă Effect Applied in Aeronautics,” *MATEC Web of Conferences*, Vol. 290, 06003, 9th International Conference on Manufacturing Science and Education, June 5-7, 2019. DOI: 10.1051/matecconf/201929006003.

[21] Fagan, A. F., L’Esperance, D., and Zaman, K. B. M. Q., “Application of a Novel Projection Focusing Schlieren System in NASA Test Facilities,” *AIAA Paper* 2014-2522, 30th AIAA Aerodynamic Measurement Technology and Ground Testing Conference, June 16-20, 2014. DOI: 10.2514/6.2014-2522.

[22] Ben-Dor, G., *Shock Wave Reflection Phenomena*, Springer, Berlin, 2nd Edition, 2007. DOI: 10.1007/978-3-540-71382-1.